

WESPR: Wind-adaptive Energy-Efficient Safe Perception & Planning for Robust Flight with Quadrotors

Khuzema Habib^{*1}, Pranav Deshakulkarni Manjunath^{*1}, Kasra Torshizi¹, Troi Williams¹, Pratap Tokekar¹

Abstract—Local wind conditions strongly influence drone performance: headwinds increase flight time, crosswinds and wind shear hinder agility in cluttered spaces, while tailwinds reduce travel time. Although adaptive controllers can mitigate turbulence, they remain unaware of the surrounding geometry that generates it, preventing proactive avoidance. Existing methods that model how wind interacts with the environment typically rely on computationally expensive fluid dynamics simulations, limiting real-time adaptation to new environments and conditions. To bridge this gap, we present *WESPR*, a fast framework that predicts how environmental geometry affects local wind conditions, enabling proactive path planning and control adaptation. Our lightweight pipeline integrates geometric perception and local weather data to estimate wind fields, compute cost-efficient paths, and adjust control strategies—all within 10 seconds. We validate *WESPR* on a Crazyflie drone navigating turbulent obstacle courses. Our results show a 12.5–58.7% reduction in maximum trajectory deviation and a 24.6% improvement in stability compared to a wind-agnostic adaptive controller.

I. INTRODUCTION

Unmanned Aerial Vehicles (UAVs) are increasingly used in agriculture, inspection, surveillance, and delivery. Quadrotors, known for agility and hovering, trade efficiency for maneuverability: unlike fixed-wing aircraft that passively generate lift, they must constantly expend thrust to maintain position and counteract disturbances.

Turbulent winds increase power demand and further degrade quadrotor stability. Larger batteries can extend their flight time, but the added weight offsets endurance gains. And modern propulsion systems also operate near peak efficiency already [1], limiting hardware improvements.

Stability is also critical for transporting sensitive payloads. However, traditional planners are wind-agnostic, only reactively dealing with wind disturbances rather than proactively avoiding them. For example, geometric controllers [2] and disturbance observers [3]–[5] improve gust tracking, but they remain fundamentally corrective.

In dense natural or urban settings, sheltered low-turbulence zones often form behind obstacles. With advancing hyperlocal sensing via NOAA HRRR [6], CBAM [7], and wind-LiDAR [8], wind-aware cost maps can be generated using Computational Fluid Dynamics (CFD) simulations. These maps penalize paths through turbulence and leverage tailwinds to reduce power consumption.

Our research explores whether current wind field priors can enable energy-efficient, safer UAV path planning. Tradi-

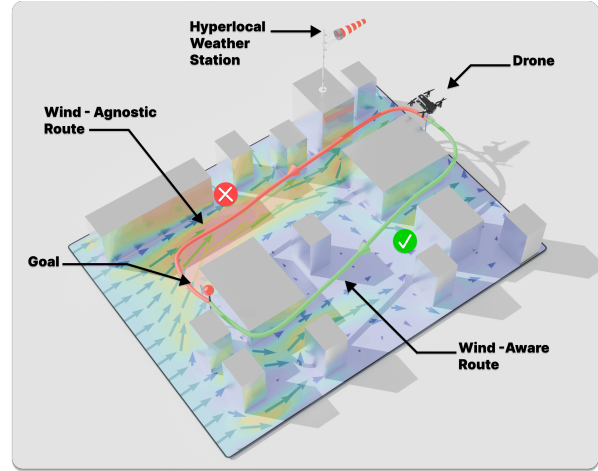


Fig. 1. A UAV navigating a turbulent environment. The red path shows the shortest route but crosses stronger winds; the green path follows a wind-aware trajectory through calmer regions.

tional CFD tools like OpenFOAM [9] are too slow for rapid deployment due to meshing and solver overhead. We instead use FluidX3D [10], a GPU-accelerated lattice Boltzmann solver that produces steady-state wind fields in seconds.

We propose *WESPR*, a pre-flight wind-aware planning framework that integrates fast CFD simulation and wind-informed optimization (Figure 1). Our paper contributes:

- Automated geometry reconstruction from overhead depth sensing.
- Rapid wind field prediction using FluidX3D with wind source priors.
- Wind-aware cost mapping based on wind velocities.
- Experimental validation showing reduced trajectory deviation and improved robustness under wind disturbances.

II. RELATED WORK

Autonomous navigation of UAVs in outdoor environments remains challenging under wind disturbances. Small quadrotors, in particular, are vulnerable due to their low mass and limited airspeed. These challenges have driven research in wind-aware planning, estimation, and disturbance-adaptive control. Here, we focus on approaches for wind-aware planning and field prediction.

A. Wind-Aware Path Planning

Wind-aware planning has been explored across geometric, sampling-based, graph-search, and optimization-based

^{*} Equal Contribution

¹ University of Maryland, College Park. {khabib, pdeshaku, ktorsh, troiw, tokekar}@umd.edu.

methods. Nonlinear guidance and geometric planners incorporate wind and vehicle constraints [11], [12], but often assume simplified or uniform wind fields. Sampling-based approaches improve feasibility under non-uniform winds from coarse global data [13], while graph-search methods such as A* and Theta* use wind-aware cost functions to reduce simulated energy use [14], yet depend on externally provided wind maps. Optimization-based planners compute energy-efficient trajectories under wind disturbances [15], [16], generally presuming known flow fields rather than predicting them from environmental geometry.

The most relevant prior work [17] demonstrated Crazyflie flight using wind-aware (CFD-informed) convex minimum-snap planning. However, the wind model was generated offline and regressed into a static field, limiting adaptability to new environments.

In contrast, WESPR extracts obstacle geometry from overhead perception and performs fast, physics-based planar wind simulation conditioned on the observed layout. The resulting flow field guides cost-aware trajectory generation. To our knowledge, no previous work combines automatic geometry extraction, physics-based wind prediction, and real-world hardware validation in a unified closed-loop pipeline.

B. Wind Estimation for UAVs

Wind estimation research primarily targets online disturbance identification at the vehicle level. EKF-based methods using drag-augmented quadrotor models estimate local wind components from onboard sensors [18]. NeuroMHE integrates neural networks with Moving Horizon Estimation for adaptive parameter tuning [5], while Contextual NeuroMHE extends generalization across wind regimes via Bayesian optimization [19]. Deep reinforcement learning has also been applied for wind-adaptive tracking with hardware validation [20]. These approaches enhance reactive disturbance rejection by estimating local wind at the vehicle state.

In contrast, WESPR predicts geometry-conditioned planar wind flow prior to execution, enabling proactive trajectory planning. Wind estimation and adaptive control methods thus complement—but do not replace—environment-conditioned flow prediction for planning.

C. Learning-Based Fluid Dynamics

Learning-based surrogates accelerate flow prediction from CFD data. CNN-based models generate near real-time wind estimates [21], and convolutional autoencoders provide rapid urban wind prediction with substantial computational speedups [22]. However, integration of such flow-prediction methods into robotic planning pipelines and validation on resource-constrained UAV hardware remains limited.

We explored neural fluid surrogates (PhysicsNeMo/DoMINO) [23], but their setup complexity and per-geometry optimization to enforce physical consistency (e.g., no-slip conditions on arbitrary STL layouts) negated inference-time gains, often requiring minutes of manual tuning per environment. We therefore employed a GPU-accelerated LBM solver that generate zero-shot, physics-verified wind fields in under 5 seconds (4 seconds on an

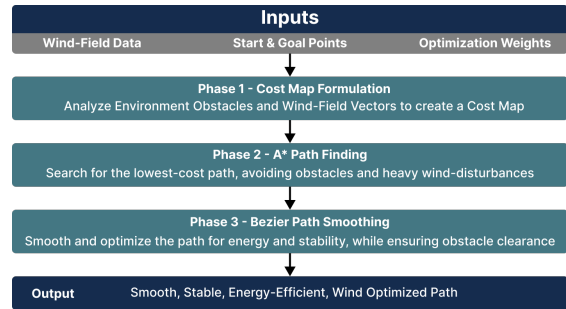


Fig. 2. The WESPR path generation pipeline as described in Section III.

RTX 3080, 6 seconds on a GTX 1650), offering reliable performance across unseen geometries.

D. Environment-Aware Robotic Control

Environment-aware control adapts to disturbances through online estimation and adaptive laws. UKF-based estimation with sliding-mode control has enabled aggressive MAV landing [24], and EKF-guided methods have achieved robust tracking under strong winds [25]. However, these reactive controllers operate at the control level and lack predictive, geometry-conditioned wind modeling for trajectory planning.

Overall, prior work has treated wind-aware planning, estimation, and adaptive control largely in isolation. To our knowledge, no unified system exists that (1) extracts obstacle geometry from perception, (2) performs physics-based planar wind-flow simulation per configuration, (3) generates wind-informed trajectories, and (4) validates tracking on physical UAVs under controlled, repeatable conditions. WESPR integrates these components into a reproducible off-board pipeline, enabling systematic evaluation of geometry-conditioned wind-aware planning.

III. THE WESPR PIPELINE

We now describe WESPR, a fast, wind field estimation and path planning pipeline (Figure 2). Our pipeline is composed of 3D Mapping and Weather Modules, a Fluid Estimation Module and a Trajectory Planning Module.

A. Obtaining a Local 3D Map and Wind Report

Our pipeline begins with obtaining a 3D map of the local environment \mathcal{M}_{3D} . The 3D map \mathcal{M}_{3D} may be represented as a point cloud or depth map, and can be obtained from prior geometric data such as city schematics, satellite imagery, or aerial surveys [26]. Next, we compute \mathcal{O} , a 2D occupancy grid, by transforming \mathcal{M}_{3D} into a bird’s eye view map, applying a depth filter to keep obstacles at or above a given altitude h_{min} , and applying post-processing to remove artifacts.

At the same time, we retrieve the wind conditions $\mathcal{W} = \{\mathbf{w}_1, \dots, \mathbf{w}_n\}$ for the local map. Each report \mathbf{w}_i contains the velocity of a wind source and its location in the map. We can obtain such reports from (hyper-)local weather stations or visual aids like wind socks.

B. Wind Field Generation Using FluidX3D

Given the \mathcal{O} and \mathcal{W} , we compute a 2D wind field \mathcal{F} using FluidX3D, a Lattice Boltzmann Method (LBM) simulator, to enable wind-aware path planning. The wind field (specifying wind speeds and directions) is defined over the discretized environment with obstacles. The simulation runs for 10,000 timesteps in about five seconds on a modern GPU and assumes a steady-state solution.

1) *Domain Construction and Boundary Conditions:* To begin computing \mathcal{F} , we automatically generate a simulation domain from the discretized 2D occupancy grid \mathcal{O} . Within \mathcal{O} , we treat occupied cells as solid nodes and free cells as fluid nodes. Then the local winds \mathcal{W} are mapped to velocity inlet boundary nodes (equilibrium node), which describe where winds enter the environment and their velocities. This representation removes the need to generate meshes, enabling automatic construction.

2) *Lattice Boltzmann Formulation:* An LBM solves the discretized Boltzmann transport equation on a Cartesian lattice [27]. The particle distribution function f_i evolves via:

$$f_i(\mathbf{x} + \mathbf{c}_i \Delta t, t + \Delta t) = f_i(\mathbf{x}, t) - \frac{\Delta t}{\tau} (f_i - f_i^{eq}), \quad (1)$$

where \mathbf{c}_i are discrete lattice velocities, τ is the relaxation time, and f_i^{eq} is the equilibrium distribution. Macroscopic values (density and velocity) are recovered through moment summation:

$$\rho = \sum_i f_i, \quad \mathbf{u} = \frac{1}{\rho} \sum_i f_i \mathbf{c}_i. \quad (2)$$

For 2D velocity discretization, we employ a D2Q9 lattice configuration. An LBM's streaming-collision structure is highly parallelizable and optimized for GPU execution, enabling near real-time wind field approximation [27].

By bypassing the complex meshing and iterative pressure-velocity coupling required by Reynolds-Averaged Navier-Stokes or Large-Eddy Simulation solvers (e.g., $k-\omega$ SST or SIMPLE), LBM significantly reduces computational latency. This efficiency makes it ideal for pre-flight wind estimation within high-speed robotics planning pipelines.

3) *Physical Scaling and Unit Interpretation:* LBM operates in lattice units, where spatial and temporal quantities are non-dimensional. Physical interpretation is obtained by scaling inlet velocities by a factor of $0.5f$ to $2f$.

Let L denote a reference length (e.g., obstacle width) and U a reference inlet wind velocity. The Reynolds number is preserved via $Re = \frac{UL}{\nu}$, where the kinematic viscosity ν is determined by the relaxation time τ . Because the objective is relative wind velocity for path planning and not high-fidelity turbulence modeling, we operate in low-to-moderate Reynolds regime, setting $Re = 250$ for our experimental conditions. The resulting wind-field provides sufficient fidelity for cost-map generation.

C. Wind-Aware Cost Map Generation

Next, we convert the 2D wind field \mathcal{F} into a cost map used for path planning (Phase 1 in Algorithm 1). The

costs penalize energetically unfavorable regions, such as strong headwinds and crosswinds, while preserving obstacle avoidance and safety margins.

1) *Projecting CFD Field onto Planning Grid:* The simulated horizontal velocity components (v_x, v_y) , the corresponding speed magnitude $s = \|\mathbf{u}\|$, and the wall mask are interpolated onto a 2D planning grid.

The resulting grid defines the domain Ω over which path planning is performed.

2) *Obstacle Representation and Safety Buffer:* The interpolated wall mask forms the initial obstacle set. A safety margin is applied by performing binary dilation with a buffer radius b (specified in meters and converted to grid cells). Additionally, domain boundary cells are marked as obstacles to prevent edge traversal.

The final obstacle set is denoted by \mathcal{O} . All cells $(i, j) \in \mathcal{O}$ are assigned a fixed large cost $C_{ij} = c_{\text{wall}}$. This ensures that the planner maintains a clearance margin from physical structures.

3) *Goal Direction:* A global unit direction vector from start to goal is computed once and is used to evaluate wind alignment across the domain.

4) *Per-Cell Flow-Aware Cost:* When wind-aware planning is enabled, each non-obstacle cell incurs a cost derived from local wind magnitude and direction. The total cell cost combines three weighted components $C_{ij} = w_s c_s + w_d c_d + w_a c_a$, where $c_s = s_{ij} / \max_{\Omega} s$ penalizes high wind speed, $c_d = 1 - (\alpha_{ij} + 1)/2$ penalizes headwinds ($\alpha_{ij} = \hat{\mathbf{u}}_{ij} \cdot \mathbf{g}$ is alignment with goal), and $c_a = 1 - |\alpha_{ij}|$ penalizes crosswinds.

The cost is clamped to $[0.1, 20]$ and smoothed with a Gaussian kernel. Obstacle cells receive a fixed penalty c_{wall} .

The key tunable parameters are: w_s : speed penalty weight, w_d : direction (headwind) penalty weight, w_a : alignment (crosswind) penalty weight, c_{wall} : obstacle penalty, and b : wall buffer distance.

When flow-aware planning is disabled, all non-obstacle cells use a constant base cost (0.5), reducing A* to Euclidean shortest-path planning (Phase 2 in Algorithm 1). For globally adverse winds (goal alignment < -0.3), the planner switches to an against-flow variant with additional edge penalties.

D. Bezier Trajectory Formulation and Optimization

The discrete waypoint sequence produced by the A* planner is refined into a dynamically smooth trajectory using a parametric Bézier curve formulation, following the approach in [17] (Phase 3 in Algorithm 1). This representation ensures continuous derivatives, bounded curvature, and compatibility with quadrotor dynamics while enabling efficient optimization.

1) *Bezier Curve Representation and Properties:* The horizontal trajectory is represented as an n^{th} -degree Bézier curve:

$$\mathbf{r}(s) = \sum_{i=0}^n B_{i,n}(s) \mathbf{P}_i, \quad s \in [0, 1], \quad (3)$$

where \mathbf{P}_0 and \mathbf{P}_n are fixed start and goal positions, and interior control points $\mathbf{P}_1, \dots, \mathbf{P}_{n-1}$ are optimization variables.

Algorithm 1 WESPR Planning Pipeline

Require: Wind field \mathbf{u}_{wind} , Start \mathbf{P}_0 , Goal \mathbf{P}_n , Weights λ
Ensure: Optimized Bézier Curve $\mathbf{r}(s)$

- 1: **Phase 1: Discrete Cost-Map Generation**
 - 2: **for** each free cell (i, j) **do**
 - 3: Calculate alignment $A = \frac{\mathbf{u} \cdot \vec{g}}{\|\mathbf{u}\|}$ and speed $V = \frac{\|\mathbf{u}\|}{\max \|\mathbf{u}\|}$
 - 4: $C_{i,j} \leftarrow \text{clamp}(w_s V + w_d(1 - \frac{A+1}{2}) + w_a(1 - |A|), 0.1, 20)$
 - 5: **end for**
 - 6: Set $C = \text{wall_penalty}$ on dilated obstacle grid \mathcal{O} .
 - 7: **Phase 2: Global Path Seeding (A*)**
 - 8: Search for discrete path \mathcal{P}_{A^*} using cost C .
 - 9: **if** Strong upstream flow ($A < -0.3$) **then**
 - 10: Apply $2.5\times$ velocity penalty to neighbor costs.
 - 11: **end if**
 - 12: **Phase 3: Continuous Bézier Optimization**
 - 13: Initialize control points $\{\mathbf{P}_1, \dots, \mathbf{P}_{n-1}\}$ from \mathcal{P}_{A^*} waypoints.
 - 14: Define objective function $J = \lambda_p J_{\text{path}} + \lambda_s J_{\text{snap}} + \lambda_t J_{\text{thrust}} + \lambda_w J_{\text{wall}}$.
 - 15: Solve for optimal control points \mathbf{P}_i via Block Coordinate Descent:
 - J_{path} : Minimize distance to \mathcal{P}_{A^*} .
 - J_{snap} : Minimize fourth-order derivative (smoothness).
 - J_{thrust} : Optimize for wind-aware energy using \mathbf{u}_{wind} .
 - J_{wall} : Enforce clearance via convex hull property.
 - 16: **return** $\mathbf{r}(s) = \sum_{i=0}^n B_{i,n}(s)\mathbf{P}_i$
-

The Bernstein basis $B_{i,n}(s) = \binom{n}{i} s^i (1-s)^{n-i}$ ensures the curve lies within the convex hull of its control points—a property exploited for collision avoidance constraints [17].

2) *Time Parameterization and Cost Functional*: The curve parameter s is mapped to physical time via $t = sT$, where T is the segment traversal time. Time derivatives scale accordingly:

$$\mathbf{v}(t) = \frac{1}{T} \frac{d\mathbf{r}}{ds}, \quad \mathbf{a}(t) = \frac{1}{T^2} \frac{d^2\mathbf{r}}{ds^2}, \quad \text{snap}(t) = \frac{1}{T^4} \frac{d^4\mathbf{r}}{ds^4}. \quad (4)$$

Following [17], the interior control points are optimized to minimize a composite cost:

$$J = \lambda_p J_{\text{path}} + \lambda_s J_{\text{snap}} + \lambda_t J_{\text{thrust}} + \lambda_w J_{\text{wall}}, \quad (5)$$

where J_{path} penalizes deviation from the A^* path, $J_{\text{snap}} = \sum \|\text{snap}(t)\|^2$ ensures dynamic smoothness, J_{wall} enforces obstacle clearance via convex-hull containment, and critically, J_{thrust} incorporates wind-aware thrust cost as derived below.

3) *Wind-Aware Thrust Cost*: As shown in [17], for a linear drag model $\mathbf{f}_d = \mathbf{K}(\mathbf{u}_{wind} - \mathbf{v})$, the thrust objective can be expressed as a quadratic form in the control points:

$$J_{\text{thrust}} = \sum_j (\mathbf{p}_j + \mathbf{v}_j)^\top \mathbf{Q}_W(T_j) (\mathbf{p}_j + \mathbf{v}_j), \quad (6)$$

where \mathbf{v}_j encodes wind information regressed from CFD data. This formulation preserves bi-convexity in control

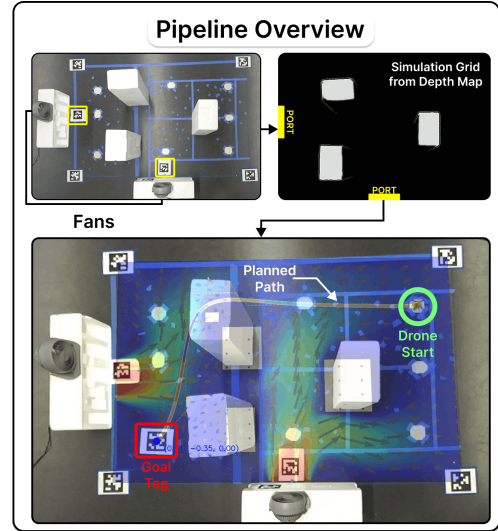


Fig. 3. Experimental pipeline. We capture an image of the environment’s physical space and the positions of the fans, obstacles, and drone’s start and goal (top left). We convert the image to an occupancy grid with fan positions (1s), and use that for our simulation (4s). Finally, we compute the drone’s path (5s) and, while the drone flies, localizes it (bottom).

points and time intervals, enabling efficient block-coordinate descent optimization [17]. Control points are initialized from A^* waypoints and constrained to local bounding boxes to maintain topological similarity while allowing refinement for wind-aware smoothness.

4) *Low-Level Flight Control*: Attitude stabilization, motor mixing, and thrust allocation are executed onboard the quadrotor firmware. The planning framework provides position and velocity setpoints, while motor commands, battery voltage, and state estimates are logged for flight analysis. Our control and tracking pipeline is shown in Figure 4.

IV. EVALUATION

We evaluated two algorithms, WESPR (ours) and `Base`, across three real-world experiments. Both algorithms utilized identical Bezier curve fitting and cost functions to optimize for smoothness, obstacle avoidance, and start-to-goal trajectory. The key difference between the algorithms was WESPR generated wind-aware trajectories, while `Base` generated wind-agnostic trajectories, where `Base` prioritized planning the shortest path. We intentionally created environments where the shortest path was more direct, but more turbulent via crosswinds or resistant via headwinds. And our objective was to determine if WESPR, a fluid-aware approach, would produce more stable, safe, and energy efficient paths compared to `Base`, a standard shortest-path planner.

1) *Physical Setup*: The 3 m x 1.8 m experimental arena consisted of an overhead camera, household fans, and styrofoam obstacles (Figure 3). Flights were performed using a Crazyflie 2.1 UAV equipped with a Flow V2 VIO sensor. To ensure localization stability, we randomly placed colored tape on the floor to enhance VIO tracking accuracy.

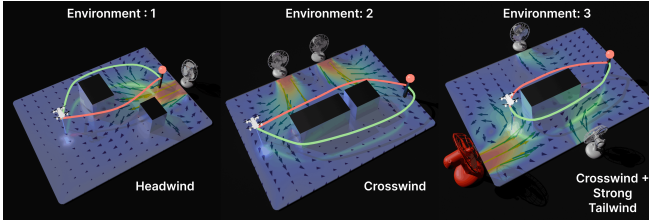


Fig. 5. 3D illustration of our three environments with the drone at the start and the red circle as the goal. The red fan represents high-speed, while the white fan represents low-speed. The Base path is shown as a red line, while the WESPR path is green. The velocities shown in each environment are relative values, not absolute.

TABLE I
FAN SPEED MEASUREMENTS OVER DISTANCE

Distance (m)	Low-Speed (m/s)	High-Speed (m/s)
0.5	4.1	5.5
1.0	3.2	3.8
1.5	1.7	2.7
3.0	0.7	1.8

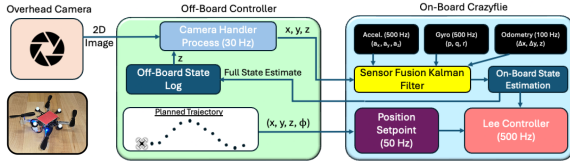


Fig. 4. We estimate the state of the Crazyflie drone by fusing odometry from its onboard Flow V2 sensor and position data from the overhead camera via HSV tracking.

We introduced controlled instability using household fans positioned along the environment’s perimeter. Table I shows the wind speed of each fan relative to a distance and power setting, which were measured by an anemometer. Styrofoam boxes (1.0x0.4x0.25 m) served as obstacles to either block or funnel wind and were oriented horizontally and vertically.

The environment data was captured using a ZED Stereo 2i camera (720p at 30 fps). We generated a map via depth filtering to find obstacles and using AprilTags to locate fan (for wind reports) and the start and goal positions. Following perspective and distortion correction, these coordinates were parsed into C++ for simulation in FluidX3D, with flow fields exported as VTK files. And during the experiments, we tracked the drone’s position via a red marker (Figure 4).

For our experiments, we created three environments (Figure 5): E1: Direct Headwind Avoidance, E2: Turbulent Crosswinds, and E3: Tailwind-Assisted Obstacle Avoidance.

V. RESULTS

To establish a performance baseline, we first evaluated both the Base and WESPR trajectories under calm conditions (“No wind”) to measure the inherent tracking error of the Lee controller. We then repeated the trials with the fans on (“Wind”), recording five flights per path. Comparing each path’s “Wind” results to its “No Wind” baseline isolates the

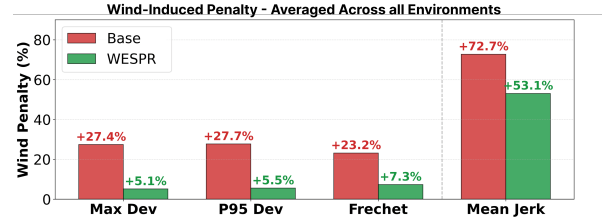


Fig. 6. Average wind-induced performance metrics across all environments (lower is better).

effect of disturbances and quantifies the resilience provided by WESPR under controlled conditions.

A. Quantitative Results

Table III shows how much each metric (maximum deviation, 95th percentile (P95) deviation, and Fréchet distance) worsens with wind for Base versus WESPR, and how much WESPR reduces that degradation relative to Base. Larger positive relative reduction (Rel. Red.) values mean WESPR is more robust in that environment and metric, keeping trajectories closer to their no-wind baseline than the Base planner. The “Val.” column represents the absolute Setpoint Tracking Error, measuring the 3D distance between the drone’s actual position and its intended reference path. We analyzed maximum and P95 deviations to evaluate susceptibility to catastrophic failure under wind disturbances [28]. To separate temporal lag from structural path divergence, we also computed the discrete Fréchet distance, which quantifies topological similarity between reference and executed trajectories [29]. Such disturbance-based analyses are standard for assessing controller robustness [30]. Under wind, WESPR consistently outperformed Base, achieving up to 58.7% lower maximum deviation, 57.9% lower P95 deviation, and a 46.9% improvement in Fréchet distance (Table III). Overall, across all trajectories and environments, the aggregate, wind-induced penalty for all metrics is significantly lower for WESPR compared to Base, as seen in Figure 6.

TABLE II
WIND-INDUCED PENALTY (%) BY ENVIRONMENT (BEST EMPHASIZED)

Env	Metric	Pen. ($\mathcal{P}_{wind}^{Base}$)	Pen. ($\mathcal{P}_{wind}^{WESPR}$)
E1	Max Dev	51.5	20.3
	P95 Dev	50.8	18.0
	Frechet	37.8	22.1
E2	Max Dev	76.8	42.8
	P95 Dev	67.4	35.1
	Frechet	97.5	50.0
E3	Max Dev	66.8	70.7
	P95 Dev	60.6	60.9
	Frechet	89.9	66.2

Wind Robustness Metrics. We quantify robustness via *Trajectory Displacement* (Δ), the maximum geometric shift between wind (\mathbf{p}_{wind}) and reference (\mathbf{p}_{no_wind}) trajectories:

$$\Delta_p = \max_t \|\mathbf{p}_{wind}^p(t) - \mathbf{p}_{no_wind}^p(t)\|_2, \quad p \in \{Base, WESPR\} \quad (7)$$

TABLE III
WESPR QUANTITATIVE PERFORMANCE COMPARISON

Env	Metric	Case	Mode	Val.(m)	Traj. Disp.(Δ ;m)	Rel.Red.(η_r , %)
E1	Max Dev	Base	No Wind	0.386	0.199	58.7%
			Wind	0.483		
	WESPR	No Wind	0.405	0.082		
		Wind	0.430			
	P95 Dev	Base	No Wind	0.336	0.171	
			Wind	0.440		
WESPR	No Wind	0.399	0.072			
	Wind	0.417				
Fréchet	Base	No Wind	0.337	0.128		
		Wind	0.440			
WESPR	No Wind	0.307	0.068			
	Wind	0.296				
E2	Max Dev	Base*	No Wind	0.297	0.228	44.3%
			Wind	0.409		
	WESPR	No Wind	0.297	0.127		
		Wind	0.314			
	P95 Dev	Base*	No Wind	0.293	0.197	
			Wind	0.386		
WESPR	No Wind	0.284	0.100			
	Wind	0.303				
Fréchet	Base*	No Wind	0.232	0.226		
		Wind	0.211			
WESPR	No Wind	0.254	0.127			
	Wind	0.301				
Max Dev	Base*	No Wind	0.389	0.260	12.5%	
		Wind	0.464			
WESPR	No Wind	0.322	0.228			
	Wind	0.332				
P95 Dev	Base*	No Wind	0.367	0.222		
		Wind	0.442			
WESPR	No Wind	0.311	0.190			
	Wind	0.327				
Fréchet	Base*	No Wind	0.278	0.250		
		Wind	0.412			
WESPR	No Wind	0.238	0.158			
	Wind	0.254				

The relative reduction (η_r) of WESPR over Base is defined as:

$$\eta_r = \frac{\Delta_{\text{Base}} - \Delta_{\text{WESPR}}}{\Delta_{\text{Base}}} \times 100\% \quad (8)$$

Second, we calculate the Wind-Induced Penalty (\mathcal{P}) for any scalar metric M (e.g., Max Deviation, Mean Jerk) to measure the relative performance degradation:

$$\mathcal{P}_{\text{wind}}^p(M) = \frac{M_{\text{wind}}^p - M_{\text{no_wind}}^p}{M_{\text{no_wind}}^p} \times 100\% \quad (9)$$

A key note regarding trajectories marked as Base* in Table III is that these trials were conducted in a *simplified environment*, where we removed obstacles in E2 and E3 or deactivated certain fans in E3. This adjustment prevented

repeated collisions caused by crosswind fans along the trajectory. Figure 7 shows that the Base path was pushed into obstacle spaces at two points, where crosswinds induced

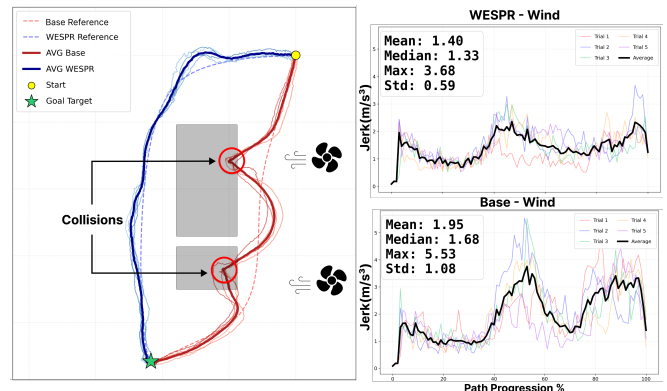


Fig. 7. (LEFT) Actual trajectories taken in E2 by the drone (faintly visible with average path in bold), WESPR (Blue) and Base (Red). Base trajectory collides with the obstacles. (RIGHT) Jerk Magnitude along the path. WESPR path is more stable with reduced max and mean jerk compared to Base.

collisions (this also happened in E3). Because a tailwind and crosswind fan on the opposite side were normally blocked by the obstacle, both were turned off when it was removed.

The consequences of neglecting aerodynamic effects are clear in the trajectory analysis of E2 (Figure 7). The Base trajectory failed under concentrated crosswinds between nearby obstacles, deviating sharply and resulting in repeated collisions. This behavior aligned with the degradation reported in Table II, where Base experiences wind-induced penalties of 76.8% for max deviation and 67.4% for the 95th Percentile Error. Because Base reacted after displacement, actuator saturation produced two distinct jerk peaks towards the middle and end of the flight (Figure 7 right). In contrast, WESPR anticipated disturbances through wind-aware optimization, completing the trajectory without collisions and achieving lower wind-induced penalties in Maximum Deviation (42.8%) and Fréchet Distance (50.0%).

To evaluate actuator effort and overall flight smoothness, we analyzed the Mean Jerk across all trajectories (Table IV). WESPR significantly reduced the control effort required to stabilize the drone under wind, with jerk reductions of 22.6% for E1 and 24.6% for E2. This effect is especially visible for the Base path in E2, where the spatial jerk profile (Figure 7) reveals severe wind-induced perturbations as it blindly battles a concentrated crosswind. By anticipating these turbulent regions, the WESPR planner prevents the onboard controller from executing the harsh reactive corrections typical of standard tracking in adverse flows.

However, WESPR exhibited a 25.5% increase in jerk under wind in E3 as it seeks local tailwinds to maximize efficiency. Although Base* had lower jerk, this trajectory was recorded without obstacles and would have resulted in collisions if they were present. In contrast, the WESPR trajectory was jerkier but collision-free. We also observed that disabling the tailwind fan immediately caused collisions, whereas no collisions occurred when it was on, indicating that the planner correctly anticipated and leveraged tailwinds to enhance overall UAV safety.

TABLE IV
COMPREHENSIVE PERFORMANCE AND DYNAMICS ANALYSIS

Env	Metric	Base	WESPR	Rel./Reduc.(%)
E1	Path Length (m)	2.785	3.211	+15.29%
	Mean Jerk (m/s^3)	1.94	1.50	+22.64%
	Collision	No	No	–
E2*	Path Length (m)	3.326	3.484	+4.75%
	Mean Jerk (m/s^3)	1.63	1.23	+24.62%
	Collision	Yes	No	–
E3*	Path Length (m)	2.878	3.170	+10.15%
	Mean Jerk (m/s^3)	1.05	1.32	-25.51%
	Collision	Yes	No	–

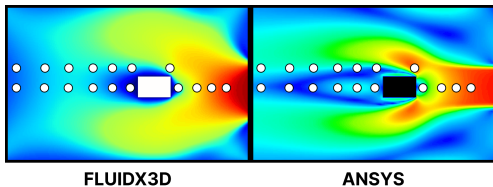


Fig. 8. Comparison of FluidX3D and Ansys Fluent configured with matching boundary conditions (Re , V_{in}), across 17 probe locations (white circles) against real-world anemometer measurements.

B. Qualitative Results

Beyond quantitative tracking accuracy, we also evaluated the end-to-end computational feasibility of the proposed pipeline. The complete WESPR pipeline executes in as little as 10 s on an NVIDIA RTX 3080, with approximately one second for environment capture, four seconds for fluid simulation, and five seconds for trajectory planning. On a lower-tier GPU (NVIDIA GTX 1650), the total runtime remains within 15 s (one second for capture, seven seconds for simulation, seven seconds for planning). These results indicate that WESPR can be integrated into existing systems with minimal computational overhead while providing meaningful improvements in safety, stability, and energy usage.

Finally, we assessed mission-level robustness in terms of collision-free completion (Table IV). While the Base planner successfully handled simple headwind scenarios, it failed in E2 and E3, where collisions occurred due to stronger wind disturbances along the path. In contrast, WESPR reached the goal in all tested environments, underscoring its effectiveness as a safety-critical planning layer for UAV operation in complex wind fields.

C. Ablations

1) *CFD Simulation Comparison*: To validate the simulation, we modeled flow around an obstacle using both Ansys Fluent and our pipeline, and compared the results with anemometer measurements in the test environment. Ansys achieved higher accuracy with an average error of ± 0.3 m/s across 17 zones, while FluidX3D (scaled by fan speed) produced ± 0.5 m/s. Despite this, the simulated flow structure was similar (Fig. 8), capturing key effects such as upstream velocity reduction and flow convergence/divergence around the obstacle. The main discrepancy was an overestimation

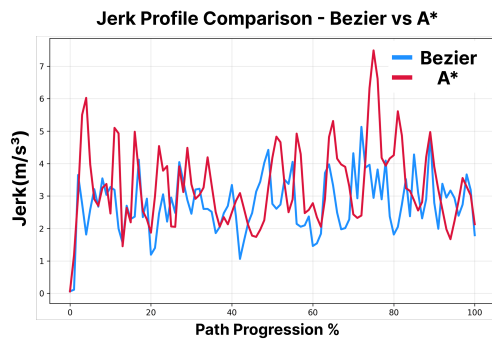


Fig. 9. A Comparison of Jerk between Bezier vs. A* Trajectory.

of velocity magnitudes in FluidX3D, which effectively introduces a conservative safety margin for planning. Some error may also arise from the linear scaling based on maximum fan speed. Given the significantly shorter runtime of our pipeline compared to the more involved Ansys workflow (manual geometry setup, meshing, and ~ 2 min solve time), this accuracy is sufficient for fast wind-aware planning.

2) *Bezier vs A* Path Stability*: We verified that Bézier smoothing has a meaningful effect on the jerk experienced by the drone (Figure 9), with nearly a 20% reduction indicating an overall smoother flight and improved tracking, especially at higher velocities. We also observed a 36% gain in reference path tracking when using the Bézier curve.

VI. CONCLUSION

In this paper, we presented WESPR, a CFD-aware trajectory planning pipeline that integrates fast Lattice Boltzmann simulations via FluidX3D into quadrotor path optimization. By embedding wind field priors directly into the cost function, WESPR generates trajectories with reduced deviation, lower jerk, improved obstacle clearance, and enhanced robustness to adverse winds compared to the geometry-only baseline Base. Our results show that lightweight, high-speed CFD solvers can provide useful aerodynamic priors for safer, more stable trajectory planning. In particular, FluidX3D’s efficiency enables near real-time flow estimation, making wind-aware optimization feasible even on modest hardware. Our validation, however, is limited to a controlled indoor setting with simplified geometry, which, while offering a repeatable proxy for wind–structure interactions, does not capture the full complexity of outdoor environments; convergence and steady-state behavior may differ in larger domains with richer boundary conditions. Nonetheless, the solver’s speed suggests that localized flow simulations can be applied incrementally over regions of interest, supporting scalable deployment.

Limitations – We faced two challenges in our pipeline: tuning the parameters for the cost functions (III-C) and Bezier curve optimization. We obtained a set of parameters for the costs experimentally and tuned them for each environment by qualitatively analyzing the generated trajectories and quantitatively comparing thrust efficiency metrics. We also only consider a single plane for a 2D simulation, instead of

3D which is more suitable for the overall path planning for a UAV. This was currently out of the scope of our evaluation as that would have required a 3D structure of the environment as well for the wind sources. However, our obstacles were uniform along their height, hence we considered only one plane for evaluation.

Future Work – We will focus on extending the framework toward fully onboard autonomy. Integrating LiDAR-based geometry reconstruction with weather-informed boundary initialization would enable online flow estimation and dynamic cost-map generation. Such a system would move toward real-time, perception-driven wind-aware navigation in complex and previously unseen environments. We will also explore learning-based methods such as Reinforcement Learning for automatic optimization of cost-function and Bezier curve parameters.

REFERENCES

- [1] D. van Niekerk, M. Case, and D. Nicolae, "Brushless direct current motor efficiency characterization," in *2015 Intl Aegean Conference on Electrical Machines & Power Electronics (ACEMP), 2015 Intl Conference on Optimization of Electrical & Electronic Equipment (OPTIM) & 2015 Intl Symposium on Advanced Electromechanical Motion Systems (ELECTROMOTION)*, 2015, pp. 226–231.
- [2] T. Lee, M. Leok, and N. H. McClamroch, "Geometric tracking control of a quadrotor uav on se (3)," in *49th IEEE conference on decision and control (CDC)*, 2010, pp. 5420–5425.
- [3] L. Bauersfeld*, E. Kaufmann*, P. Foehn, S. Sun, and D. Scaramuzza, "Neurobom: Hybrid aerodynamic quadrotor model," in *Robotics: Science and Systems XVII*, ser. RSS2021. Robotics: Science and Systems Foundation, Jul. 2021. [Online]. Available: <http://dx.doi.org/10.15607/RSS.2021.XVII.042>
- [4] L. Bauersfeld and G. J. J. Ducard, "Mpc-based control of a quadrotor uav for precise trajectory tracking in turbulent wind," *IEEE Control Systems Letters*, vol. 5, no. 6, pp. 1892–1897, 2021.
- [5] B. Wang, Z. Ma, S. Lai, and L. Zhao, "Neural moving horizon estimation for robust flight control," *IEEE Transactions on Robotics*, vol. 40, pp. 639–659, 2024.
- [6] E. P. James, C. R. Alexander, D. C. Dowell, S. S. Weygandt, S. G. Benjamin, G. S. Manikin, J. M. Brown, J. B. Olson, M. Hu, T. G. Smirnova *et al.*, "The high-resolution rapid refresh (hrrr): an hourly updating convection-allowing forecast model. part ii: Forecast performance," *Weather and Forecasting*, vol. 37, no. 8, pp. 1397–1417, 2022.
- [7] S. Davis, P. Pithani, A. Pattantyus, M. Marchand, S. Flampouris, and L. Peffers, "Comprehensive Bespoke Atmospheric Model (CBAM)'s High Resolution Reanalysis Dataset By Tomorrow.Io for Supporting Climate Resilient Crop Varieties in Sub-Saharan Africa," in *104th Annual AMS Meeting 2024*, ser. American Meteorological Society Meeting Abstracts, vol. 104, Jan. 2024, p. 431465.
- [8] S. Nabi, N. Nishio, P. Grover, R. Matai, Y. Kajiyama, N. Kotake, S. Kameyama, W. Yoshiki, and M. Iida, "Improving lidar performance on complex terrain using cfd-based correction and direct-adjoint-loop optimization," in *Journal of Physics: Conference Series*, vol. 1452, no. 1. IOP Publishing, 2020, p. 012082.
- [9] H. Jasak, A. Jemcov, Z. Tukovic *et al.*, "Openfoam: A c++ library for complex physics simulations," in *International workshop on coupled methods in numerical dynamics*, vol. 1000, 2007, pp. 1–20.
- [10] M. Lehmann, "Fluidx3d: A very fast and massive parallel lattice boltzmann code," *Journal of Open Source Software*, vol. 7, no. 70, p. 4018, 2022.
- [11] L. Furieri, T. Stastny, L. Marconi, R. Siegwart, and I. Gilitschenski, "Gone with the wind: Nonlinear guidance for small fixed-wing aircraft in arbitrarily strong windfields," in *2017 American Control Conference (ACC)*, 2017, pp. 4254–4261.
- [12] S. Schopferer and T. Pfeifer, "Performance-aware flight path planning for unmanned aircraft in uniform wind fields," in *2015 International Conference on Unmanned Aircraft Systems (ICUAS)*, 2015, pp. 1138–1147.
- [13] P. Oettershagen, F. Achermann, B. Müller, D. Schneider, and R. Y. Siegwart, "Towards fully environment-aware uavs: Real-time path planning with online 3d wind field prediction in complex terrain," *ArXiv*, vol. abs/1712.03608, 2017. [Online]. Available: <https://api.semanticscholar.org/CorpusID:24168247>
- [14] R. GU, Y. ZHAO, and X. REN, "Integrating wind field analysis in uav path planning: Enhancing safety and energy efficiency for urban logistics," *Chinese Journal of Aeronautics*, vol. 39, no. 1, p. 103605, 2026. [Online]. Available: <https://www.sciencedirect.com/science/article/pii/S1000936125002110>
- [15] S. Gasche, C. Kallies, A. Himmel, and R. Findeisen, "Energy aware and safe path planning for unmanned aircraft systems," *arXiv preprint arXiv:2504.03271*, 2025.
- [16] P. Abichandani, D. Lobo, M. Muralidharan, N. Runk, W. McIntyre, D. Bucci, and H. Benson, "Distributed motion planning for multiple quadrotors in presence of wind gusts," *Drones*, vol. 7, no. 1, 2023. [Online]. Available: <https://www.mdpi.com/2504-446X/7/1/58>
- [17] Y. Huang, M. Greiff, A. Vinod, and S. Di Cairano, "Leveraging computational fluid dynamics in uav motion planning," in *2024 American Control Conference (ACC)*, 2024, pp. 375–381.
- [18] L. Sikkil, G. de Croon, C. De Wagter, and Q. Chu, "A novel online model-based wind estimation approach for quadrotor micro air vehicles using low cost mems imus," in *2016 IEEE/RSJ International Conference on Intelligent Robots and Systems (IROS)*, 2016, pp. 2141–2146.
- [19] K. Torshizi, C. L. Shek, K. Habib, G. Shi, P. Tokekar, and T. Williams, "Contextual neural moving horizon estimation for robust quadrotor control in varying conditions," *arXiv preprint arXiv:2509.24281*, 9 2025.
- [20] B. Ma, Z. Liu, Q. Dang, W. Zhao, J. Wang, Y. Cheng, and Z. Yuan, "Deep reinforcement learning of uav tracking control under wind disturbances environments," *IEEE Transactions on Instrumentation and Measurement*, vol. 72, pp. 1–13, 2023.
- [21] F. Achermann, N. R. J. Lawrence, R. Ranftl, A. Dosovitskiy, J. J. Chung, and R. Siegwart, "Learning to predict the wind for safe aerial vehicle planning," in *2019 International Conference on Robotics and Automation (ICRA)*, 2019, pp. 2311–2317.
- [22] G. Veiga-Piñeiro, E. Aldao-Pensado, and E. Martín-Ortega, "Hybrid cfd-deep learning approach for urban wind flow predictions and risk-aware uav path planning," *Drones*, vol. 9, no. 11. [Online]. Available: <https://www.mdpi.com/2504-446X/9/11/791>
- [23] PhysicsNeMo Contributors, "NVIDIA PhysicsNeMo: An Open-Source Framework for Physics-Based Deep Learning in Science and Engineering," <https://github.com/NVIDIA/physicsnemo>, 2023, released February 24, 2023.
- [24] A. Paris i Bordas, "Control and estimation strategies for autonomous mav landing on a moving platform in turbulent wind conditions," Ph.D. dissertation, Massachusetts Institute of Technology, 2020.
- [25] T. Stastny and R. Y. Siegwart, "On flying backwards: Preventing run-away of small, low-speed, fixed-wing uavs in strong winds," *2019 IEEE/RSJ International Conference on Intelligent Robots and Systems (IROS)*, pp. 5198–5205, 2019. [Online]. Available: <https://api.semanticscholar.org/CorpusID:199442199>
- [26] T. Sasaki, K. Otsu, R. Thakker, S. Haesaert, and A.-a. Aghamohammadi, "Where to map? iterative rover-copter path planning for mars exploration," *IEEE Robotics and Automation Letters*, vol. 5, no. 2, pp. 2123–2130, 2020.
- [27] M. Lehmann, M. J. Krause, G. Amati, M. Sega, J. Harting, and S. Gekle, "Accuracy and performance of the lattice boltzmann method with 64-bit, 32-bit, and customized 16-bit number formats," *Phys. Rev. E*, vol. 106, p. 015308, Jul 2022. [Online]. Available: <https://link.aps.org/doi/10.1103/PhysRevE.106.015308>
- [28] M. Ono and B. C. Williams, "Iterative risk allocation: A new approach to robust model predictive control with a joint chance constraint," in *2008 47th IEEE Conference on Decision and Control*, 2008, pp. 3427–3432.
- [29] H. Alt and M. GODAU, "Computing the fréchet distance between two polygonal curves," *Int. J. Comput. Geometry Appl.*, vol. 5, pp. 75–91, 03 1995.
- [30] M. B. Abdelghany, A. M. Moustafa, and M. Moness, "Benchmarking tracking autopilots for quadrotor aerial robotic system using heuristic nonlinear controllers," *Drones*, vol. 6, no. 12, 2022. [Online]. Available: <https://www.mdpi.com/2504-446X/6/12/379>